CHINESE OPTICS LETTERS

Vol. 19, No. 8 | August 2021

External focusing dependence of spatial distribution of air lasers during femtosecond laser filamentation in air

Jiayun Xue (薛嘉云)[1,†], Hui Gao (高 慧)[2,†], Nan Zhang (张 楠)[1], Lu Sun (孙 陆)[1], Lie Lin (林 列)[1], and Weiwei Liu (刘伟伟)[1*]

[1] Institute of Modern Optics, Tianjin Key Laboratory of Micro-Scale Optical Information Science and Technology, Nankai University, Tianjin 300350, China

[2] School of Physical Science and Technology, Tiangong University, Tianjin 300387, China

*Corresponding author: liuweiwei@nankai.edu.cn

Received December 21, 2020 | Accepted February 2, 2021 | Posted Online April 28, 2021

The spatial distribution of the forward-propagating amplified spontaneous emission (ASE) of nitrogen molecular ions during femtosecond laser filamentation in air is studied via numerical simulations. The results suggest that the divergence angle and signal intensity are extremely sensitive to the external focal length. Concurrently, we show that the optical Kerr effect plays a significant role in concentrating the directivity of ASE signals, particularly in cases of loose focusing. Furthermore, the simulations demonstrate that ASE signals are enhanced for a tight focus, although the corresponding filament length is shorter. The main physical mechanism underlying this process is the competition between the plasma defocusing and optical Kerr effects. The result is important for filamentation-based light detection and ranging applied to remote sensing.

Keywords: air laser; amplified spontaneous emission; femtosecond laser filamentation.

DOI: 10.3788/COL202119.081402

1. Introduction

Femtosecond laser filamentation-based light detection and ranging (lidar) represents an attractive new technique for the remote sensing of air pollutants[1,2]. The popularity of this technique lies in the fact that the laser intensity inside a light filament exceeds 10^{13} W/cm^2 as the laser propagates in air[3]. Many substances, including gases[4], aerosols[5], dusts[6], and metals[7], will be ionized under such high intensity, followed by the emission of a fluorescence fingerprint spectrum. In addition, amplified spontaneous emission (ASE) has been widely reported during filamentation, including for nitrogen molecules[8], oxygen atoms[9], and neutral fragments of CH[4], OH[10], and NH[11]. This has the benefit of either enhancing the fluorescence signal in the backward direction or remote laser amplification in the forward direction when a seed pulse is used[12,13]. This unique phenomenon has been widely referred to as an "air laser"[8–10,12–16]. It is worth noting that for remote applications in open air, the lasing action could be realized by either self-seeded lasing from femtosecond laser filaments or white light seeded multiple wavelength lasing[13,15,17].

Recently, air lasers with different spatial profiles have been demonstrated experimentally. Air lasing of oxygen atoms at the wavelength of 845 nm produces a donut shape with a divergence angle of 40 mrad[9]. Elsewhere, backward UV lasing at 337 nm and 357 nm from nitrogen molecules has been reported to give rise to a roughly super-Gaussian profile with a divergence angle of 1.6 mrad[14]. In addition, gas pressure has been found to have a significant effect on the signal intensity and spatial profile of air lasers. Spatial profiles of forward self-seeded lasing from nitrogen ions have been observed as Gaussian patterns, morphing to an outer ring structure when the gas pressure increases. The corresponding divergence angle was measured as approximately 20 mrad[15]. The mechanism of spatial distribution is still unclear.

In this study, we use numerical simulations to elucidate the spatial distribution in the forward direction for the example of an air laser of nitrogen molecular ions at 391 nm. The results reveal that the spatial distribution of the air laser depends heavily on external focusing. This is attributed to the competition between the plasma defocusing and optical Kerr effects. Our study provides a theoretically feasible method for improving the energy conversion efficiency, signal-to-noise ratio, and directivity of air laser, which is important for filament-based lidar applied to remote sensing of air pollutants.

2. Numerical Simulation Method

Numerical simulations are based on the following nonlinear wave equation[18]:

$$-2ik\frac{\partial A}{\partial z} = \Delta_{\perp}A + 2\frac{k^2}{n_0}n_{\mathrm{nl}}A - ik\alpha A, \tag{1}$$

where $\Delta_{\perp}$ denotes the transverse Laplacian operator, z represents the light propagation distance, A represents the envelope

of the laser amplitude, and k is the wave number of the laser given by $k = n_0\omega_0/c_0$ (ω_0 and c_0 are the angular frequency of the laser and the speed of light in a vacuum, respectively). Additionally, n_0 indicates the linear refractive index of air, while n_{nl} denotes the nonlinear refractive index inside the filament.

The simulations consisted of two steps. In the first step, the nonlinear propagation of the fundamental laser was conducted to describe the filamentation process. In this case, the influences of energy loss and amplification were not considered in the simulation, that is, $\alpha = 0$ in Eq. (1). Therefore, the first step can be used to obtain the spatial distribution of the plasma density. In the second step, the propagation of the air laser was simulated based on the spatial distribution of the plasma density. In the air laser simulation, $\alpha > 0$ represents the amplification of fluorescence along the propagation direction.

Considering that nitrogen ions are regarded as the gain media for nitrogen fluorescence, the gain along the propagation path is related to the nitrogen ion density distribution[19]. In our simulation, the gain coefficient along the propagation direction is proportional to the stimulated emission cross section, σ, and the nitrogen ion density, $N_e^{N_2^+}$[20,21]:

$$\alpha = N_e^{N_2^+}\sigma(\upsilon). \tag{2}$$

According to a previous study[22], the transition cross section for the (0-0) vibrational transition of the first negative band (at $\lambda = 391.4\,\mathrm{nm}$) was determined to be $14.8 \times 10^{-18}\,\mathrm{cm}^2$. It is worth mentioning that a similar method has been successfully used in Refs. [21,23] to discuss the development of the remote atmospheric lasing at 337 nm.

3. Result and Discussion

In our simulation, the wavelength of the fundamental laser was centered at 800 nm with a beam radius ($1/e^2$) of 5 mm and a pulse duration (FWHM) of 60 fs. The laser pulse energy was set to 6 mJ. Corresponding to initial filament positions of $z = 0.2$, 1.0, and 10.0 m, the external focal length was chosen as $f = 0.2$, 1.0, and 34 m, respectively. Note that the propagation distance z denotes the distance from the focusing lens.

Furthermore, due to the high clamped intensity inside the filament, neutral N_2 is ionized to N_2^+ through multiphoton/tunnel ionization. The ground state ($X^2\Sigma_g^+$) ion is pumped to the excited state ($B^2\Sigma_u^+$) by the nonlinear physical process inside the filament instantaneously[24]. The fluorescence of N_2^+ at 391 nm was assigned as the (0-0) vibrational transition of the first negative band ($B^2\Sigma_u^+ \rightarrow X^2\Sigma_g^+$). The initial intensity distribution of ASE was simulated as follows. First, the initial fluorescence was generated at the location where the density of nitrogen ions exceeds a threshold of $10^{15}\,\mathrm{cm}^{-3}$. The initial photon density $N_{391\,\mathrm{nm}}$ is given by[23]

$$N_{391\,\mathrm{nm}} = N_e^{N_2^+} W_{21}\tau, \tag{3}$$

which depends on the nitrogen ion density $N_e^{N_2^+}$, the probability of stimulated emission W_{21}, and the population inversion lifetime τ. As indicated by a previous experiment, τ is approximately 46.2 ps[25]. Furthermore, W_{21} is related to the spectral energy density of blackbody radiation and the Einstein B-coefficient[20]:

$$W_{21} = B_{21}\frac{8\pi h\nu^3}{c_0^3}\frac{1}{e^{h\nu/k_BT} - 1}, \tag{4}$$

where ν, h, and k_B represent the frequency of the stimulated emission, Planck's constant, and Boltzmann's constant, respectively. In addition, T denotes the electron temperature inside the filament, which, according to the Boltzmann method, is approximately 6200 K[26]. Next, the Einstein B-coefficient, B_{21}, was calculated according to the relation with the Einstein A-coefficient, A_{21}[20]:

$$\frac{B_{21}}{A_{21}} = \frac{c_0^3}{8\pi h\nu^3}. \tag{5}$$

The probability of spontaneous emission A_{21} for the N_2^+ first negative system of (0-0) at 391 nm is $1.1 \times 10^7\,\mathrm{s}^{-1}$[27].

Figures 1(a1)–1(a3) present the spatial distributions of the nitrogen ion density corresponding to $f = 0.2$, 1.0, and 34 m, respectively. These simulations demonstrate that the filament length increases with the increasing external focus length, changing from 2 cm [Fig. 1(a1)] to 15 cm [Fig. 1(a2)] and 50 cm [Fig. 1(a3)]. It is worth mentioning that, as described in Ref. [28], the peak plasma density inside the filament is highly sensitive to the external focal conditions. Our numerical simulations agree closely with previous observations[28]. Under a tight focus of $f = 10\,\mathrm{cm}$, the plasma density reaches $10^{18}\,\mathrm{cm}^{-3}$, which is almost three orders of magnitude higher than that when $f = 34\,\mathrm{m}$.

In addition, the simulated spatial distributions of the forward air lasers are displayed in Figs. 1(b1)–1(c3). These simulations reveal that significant gain exists inside the filament. After the filament, the air laser diverges. However, it is interesting to note that the divergent angle of the air laser reduces when the Kerr effect is considered in the numerical simulation, especially for longer filaments [Figs. 1(b2) and 1(b3)]. Figure 2 further highlights this trend.

Figure 2(a) plots the signal intensity as a function of the divergent angle for a focal length $f = 0.2\,\mathrm{m}$, demonstrating that the signal intensity and spatial distribution of the air laser exhibit negligible difference in response to considering the Kerr effect. However, for long focal lengths, as demonstrated in Figs. 2(b) and 2(c), the Kerr effect strengthens the signal intensity significantly. Moreover, in these cases, the Kerr effect acts to concentrate the air laser energy more tightly around the propagation axis, as shown in Fig. 2(d). The corresponding divergent angles become smaller as the focal length increases. Specifically, when $f = 1.0\,\mathrm{m}$, the divergent angles are approximately 0.75 mrad [with the Kerr effect, black solid line in Fig. 2(b)] and 1 mrad

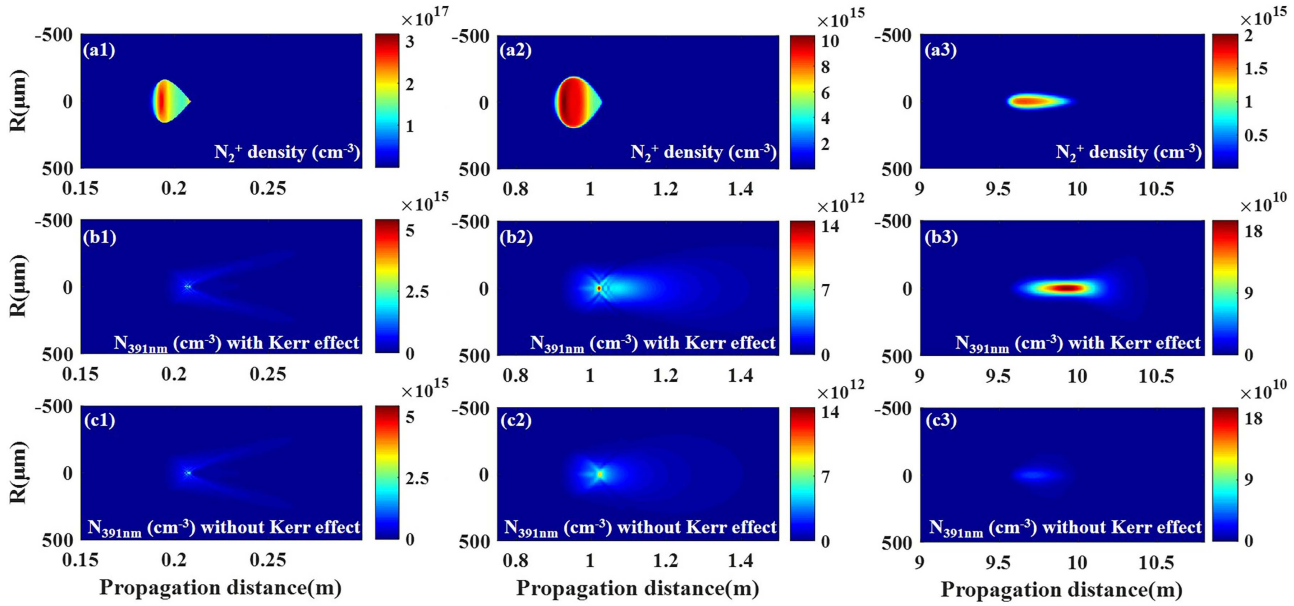

Fig. 1. Spatial distributions of (a) nitrogen ion density induced by the filament and (b), (c) the photon density of air lasers (with and without the Kerr effect, respectively) for different external focusing conditions: (a1), (b1), (c1) $f = 0.2$ m; (a2), (b2), (c2) $f = 1$ m; (a3), (b3), (c3) $f = 34$ m.

[without the Kerr effect, red dashed line in Fig. 2(b)]. As depicted in Fig. 2(c), for $f = 34.0$ m, the corresponding values are 0.98 mrad and 3.37 mrad, respectively. Our simulation result is approximate to the divergence angle of 1.6 mrad measured in the experiment[14].

The results outlined in Fig. 2(a) confirm that, for tight focusing, the external focusing dominates the propagation of the pump laser[28,29]. Most of the laser energy is confined within a small filament zone, as well as the plasma. Because the plasma density inside the filament is sufficiently large, the effect of plasma defocusing becomes much stronger than the Kerr effect. Diffraction caused by the plasma plays a major role during the propagation of the air laser. As a result, the air laser diffracts immediately outside of the filament, with the Kerr effect no longer participating in its propagation. The ring-shaped air laser pattern in Fig. 2(a) illustrates the effect of plasma defocusing. A similar result of a ring structure has also been observed experimentally[15,17]. It was also induced by the plasma defocusing effect when the plasma density increases with the increase of gas pressure. However, for looser focusing, as shown in Figs. 1(b3) and 1(c3), the laser intensity is lower than those in Figs. 1(b1) and 1(c1). A significantly reduced plasma density results in substantially weaker diffraction, which slows the energy leakage from the filament. Hence, the Kerr effect should be considered over longer distances. The weaker divergence exhibited in Fig. 2(c) reflects this fact. Figure 2(d) further illustrates the abovementioned phenomenon. In general, as a result of counterbalancing between the Kerr effect and plasma defocusing, the divergent angle of the air laser decreases as the external focal length increases. When the focal length of the lens exceeds 2 m, which corresponds to a numerical aperture of approximately 0.005, the divergence becomes almost invariant.

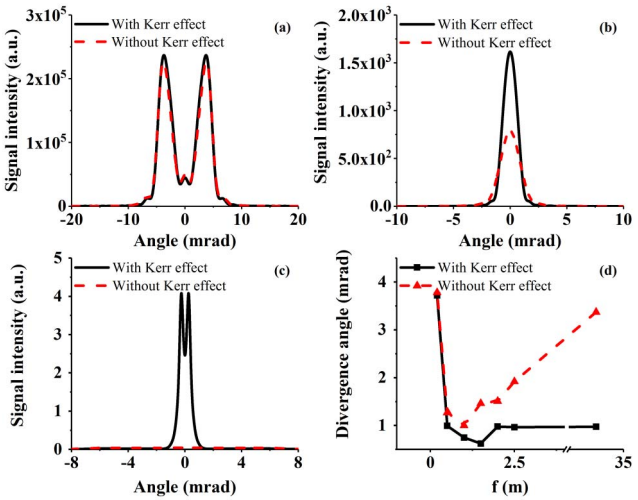

Fig. 2. Far-field angular distribution of the air laser for (a) $f = 0.2$ m, (b) $f = 1$ m, and (c) $f = 34$ m. (d) Divergence angle of the air laser as a function of the external focusing length.

Moreover, the energy of the air laser along the propagation direction can be interpreted using the simulated phonon density at 391 nm. The corresponding results are shown in Figs. 3(a)–3(c). The plots show that the energy of the air laser experiences a gain inside the filament region and then settles at a constant level in the post-filament region. For short focal lengths, little difference between the total energies is observed for the cases with and without the Kerr effect, as shown in Figs. 3(a) and 3(b). However, for the loose focus in Fig. 3(c), the Kerr effect is considered, resulting in a higher energy (by 10^{-4} nJ) than that when the Kerr effect is not taken into account. This indicates that the Kerr effect plays a relatively more obvious role at longer focal lengths. With the Kerr effect, the air laser is

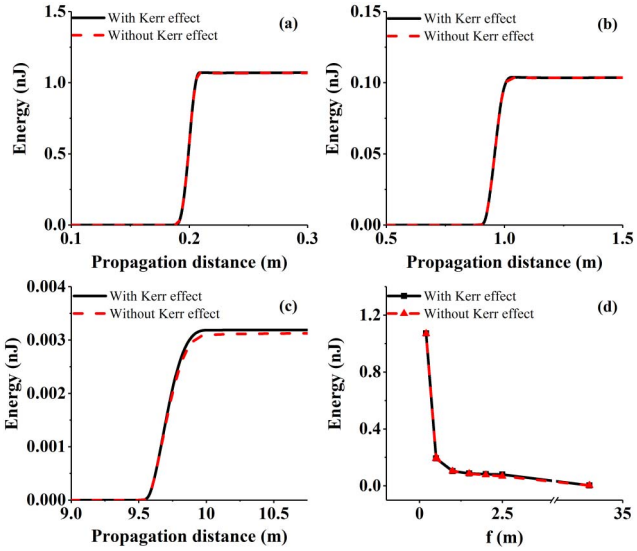

Fig. 3. Energy of the air laser along the propagation direction for external focus of (a) $f = 0.2$ m, (b) $f = 1$ m, and (c) $f = 34$ m. (d) Air laser energy as a function of the external focal length.

focused more tightly around the propagation axis, with a higher intensity than that for off-axis propagation. Considering the nitrogen ion density distribution, increased density close to the propagation axis leads to a greater exponential amplification. Therefore, the energy of the air laser is enhanced when the Kerr effect is considered. Figure 3(d) presents the air laser energy as a function of the external focus length.

In addition to the energy difference observed when the Kerr effect is switched on and off, the air laser energy also shows a strong dependence on the external focusing. For $f = 0.2$ m, the energy of the air laser is approximately 1.07 nJ, which is more than 300 times greater than that when $f = 34$ m. For a shorter focal length, the peak plasma density[28] and the nitrogen ion density within the filament are higher, as evidenced by Figs. 1(a1)–1(a3). According to Eq. (2), the gain coefficient is larger at shorter focal lengths. As a result of the exponential growth of fluorescence intensity inside the filament region, the total energy of the air laser generated with a short focal condition is higher than that with a long focal condition.

4. Conclusion

In summary, we performed numerical simulation of the generation and forward propagation of an air laser at 391 nm during femtosecond laser filamentation, which is identified as the transmission of the first negative (0-0) band of nitrogen ions. The results indicate that the optical Kerr effect has a significant influence on the far-field divergence angle, helping to maintain the directivity of the air laser. Furthermore, the energy and far-field divergence angle of the air laser depend strongly on the external focus. An optimal initial pump energy and lens focal length are selected, resulting in an air laser with high directivity, intensity, and energy conversion efficiency. Our study provides a valuable theoretical basis for improving the energy conversion efficiency and signal-to-noise ratio of air lasers, which are significant factors for remote sensing applications.

Acknowledgement

This work was supported by the National Key R&D Program of China (No. 2018YFB0504400).

†These authors contributed equally to this work.

References

1. I. Dicaire, V. Jukna, C. Praz, C. Milian, L. Summerer, and A. Couairon, "Spaceborne laser filamentation for atmospheric remote sensing," Laser Photon. Rev. **10**, 481 (2016).
2. H. Xu, Y. Cheng, S. L. Chin, and H. Sun, "Femtosecond laser ionization and fragmentation of molecules for environmental sensing," Laser Photon. Rev. **9**, 275 (2015).
3. W. Liu, "Intensity clamping during femtosecond laser filamentation," Chin. J. Phys. **52**, 465 (2014).
4. S. A. Hosseini, A. Azarm, J. F. Daigle, Y. Kamali, and S. L. Chin, "Filament-induced amplified spontaneous emission in air–hydrocarbons gas mixture," Opt. Commun. **316**, 61 (2014).
5. J. F. Daigle, G. Méjean, W. Liu, F. Théberge, H. L. Xu, Y. Kamali, J. Bernhardt, A. Azarm, Q. Sun, P. Mathieu, G. Roy, J. R. Simard, and S. L. Chin, "Long range trace detection in aqueous aerosol using remote filament-induced breakdown spectroscopy," Appl. Phys. B **87**, 749 (2007).
6. H. L. Xu, G. Méjean, W. Liu, Y. Kamali, J. F. Daigle, A. Azarm, P. T. Simard, P. Mathieu, G. Roy, J. R. Simard, and S. L. Chin, "Remote detection of similar biological materials using femtosecond filament-induced breakdown spectroscopy," Appl. Phys. B **87**, 151 (2007).
7. W. Liu, H. L. Xu, G. Méjean, Y. Kamali, J. F. Daigle, A. Azarm, P. T. Simard, P. Mathieu, G. Roy, and S. L. Chin, "Efficient non-gated remote filament-induced breakdown spectroscopy of metallic sample," Spectrochim. Acta Part B **62**, 76 (2007).
8. Q. Luo, W. Liu, and S. L. Chin, "Lasing action in air induced by ultrafast laser filamentation," Appl. Phys. B **76**, 337 (2003).
9. A. Dogariu, J. B. Michael, M. O. Scully, and R. B. Miles, "High-gain backward lasing in air," Science **331**, 442 (2011).
10. S. Yuan, T. Wang, Y. Teranishi, A. Sridharan, S. H. Lin, H. Zeng, and S. L. Chin, "Lasing action in water vapor induced by ultrashort laser filamentation," Appl. Phys. Lett. **102**, 224102 (2013).
11. S. Yuan, T. Wang, P. Lu, S. L. Chin, and H. Zeng, "Humidity measurement in air using filament-induced nitrogen monohydride fluorescence spectroscopy," Appl. Phys. Lett. **104**, 091113 (2014).
12. J. Ni, W. Chu, C. Jing, H. Zhang, B. Zeng, J. Yao, G. Li, H. Xie, C. Zhang, H. Xu, S.-L. Chin, Y. Cheng, and Z. Xu, "Identification of the physical mechanism of generation of coherent N^{2+} emissions in air by femtosecond laser excitation," Opt. Express **21**, 8746 (2013).
13. J. Yao, B. Zeng, H. Xu, G. Li, W. Chu, J. Ni, H. Zhang, S. L. Chin, Y. Cheng, and Z. Xu, "High-brightness switchable multiwavelength remote laser in air," Phys. Rev. A **84**, 051802 (2011).
14. D. Kartashov, S. Alisauskas, G. Andriukaitis, A. Pugžlys, M. N. Shneider, A. M. Zheltikov, S. L. Chin, and A. Baltuska, "Free-space nitrogen gas laser driven by a femtosecond filament," Phys. Rev. A **86**, 033831 (2012).
15. Y. Liu, Y. Brelet, G. Point, A. Houard, and A. Mysyrowicz, "Self-seeded lasing in ionized air pumped by 800 nm femtosecond laser pulses," Opt. Express **21**, 22791 (2013).
16. D. Zhou, X. Zhang, Q. Lu, Q. Liang, and Y. Liu, "Time-resolved study of the lasing emission from high vibrational levels of N_2^+," Chin. Opt. Lett. **18**, 023201 (2020).

17. W. Chu, G. Li, H. Xie, J. Ni, J. Yao, B. Zeng, H. Zhang, C. Jing, H. Xu, and Y. Cheng, "A self-induced white light seeding laser in a femtosecond laser filament," Laser Phys. Lett. **11**, 015301 (2014).
18. A. Chiron, B. Lamouroux, R. Lange, J. F. Ripoche, M. Franco, B. Prade, G. Bonnaud, G. Riazuelo, and A. Mysyrowicz, "Numerical simulations of the nonlinear propagation of femtosecond optical pulses in gases," Eur. Phys. J. D **6**, 383 (1999).
19. T. Zeng, J. Zhao, W. Liu, and S. L. Chin, "Backward angular distribution of air lasing induced by femtosecond laser filamentation," Laser Phys. Lett. **11**, 075401 (2014).
20. B. Saleh, M. Teich, and R. E. Slusher, *Fundamentals of Photonics* (Wiley, 1991).
21. P. Sprangle, J. Peñano, B. Hafizi, D. Gordon, and M. Scully, "Remotely induced atmospheric lasing," Appl. Phys. Lett. **98**, 211102 (2011).
22. J. P. Doering and J. Yang, "Comparison of the electron impact cross section for the N_2^+ first negative (0,0) band (λ3914 Å) measured by optical fluorescence, coincidence electron impact, and photoionization experiments," J. Geophys. Res. **101**, 19723 (1996).
23. D. Kartashov and M. N. Shneider, "Femtosecond filament initiated, microwave heated cavity-free nitrogen laser in air," J. Appl. Phys. **121**, 113303 (2017).
24. S. L. Chin, H. Xu, Y. Cheng, Z. Xu, and K. Yamanouchi, "Natural population inversion in a gaseous molecular filament," Chin. Opt. Lett. **11**, 013201 (2013).
25. J. Yao, G. Li, C. Jing, B. Zeng, W. Chu, J. Ni, H. Zhang, H. Xie, C. C. Zhang, and H. Li, "Remote creation of coherent emissions in air with two-color ultrafast laser pulses," New J. Phys. **15**, 023046 (2013).
26. W. Liu, J. Bernhardt, F. Theberge, S. L. Chin, M. Châteauneuf, and J. Dubois, "Spectroscopic characterization of femtosecond laser filament in argon gas," J. Appl. Phys. **102**, 033111 (2007).
27. D. E. Shemansky and A. L. Broadfoot, "Excitation of N_2 and N_2^+ systems by electrons—I. Absolute transition probabilities," J. Quant. Spectrosc. Radiat. Transf. **11**, 1385 (1971).
28. F. Theberge, W. Liu, P. T. Simard, A. Becker, and S. L. Chin, "Plasma density inside a femtosecond laser filament in air: strong dependence on external focusing," Phys. Rev. E **74**, 036406 (2006).
29. K. Lim, M. Durand, M. Baudelet, and M. Richardson, "Transition from linear- to nonlinear-focusing regime in filamentation," Sci. Rep. **4**, 7217 (2014).